Traceable stopping cross sections of Al and Mo elemental targets for 0.9–3.6-MeV protons

M. V. Moro,* T. F. Silva, A. Mangiarotti, Z. O. Guimarães-Filho, M. A. Rizzutto, N. Added, and M. H. Tabacniks
Institute of Physics, University of São Paulo, Rua do Matão 1371, 05508-090, São Paulo, Brazil
(Received 23 November 2015; published 8 February 2016)

Accurate knowledge about the energy loss of ions in matter is essential in many problems, ranging from fundamental to applied nuclear physics. Indeed, there is a recent and increasing demand for new data on stopping cross sections measured with high accuracy and with a rigorous budget of their uncertainty sources. In the present paper we describe an accurate and traceable approach to determine the stopping cross sections in pure elemental materials—aluminum and molybdenum—for protons in the energy range of 0.9–3.6 MeV by the transmission method. The main sources of uncertainties here considered are (i) (random) the uncertainty in the peak positions and in the Gaussian fits and (ii) (systematic) the presence of thickness nonuniformity (a special procedure has been developed to correct it as far as possible). The accuracy in the final stopping cross section is 0.63% (0.32% random and 0.54% systematic) for Al and 1.5% (0.44% random and 1.4% systematic) for Mo, both mainly limited by the quality and homogeneity of the foils. For Al, this high accuracy represents an improvement compared to previous publications and serves as a benchmark for our procedure. For Mo, even though the uncertainty is somewhat higher, our results will help in improving the few data currently available in the energy range here considered. The data were also compared to the most commonly employed theoretical models (SRIM 1985, SRIM 2013, PSTAR, and CASP 5.2) and Monte Carlo codes (GEANT 3 and GEANT 4). The experimental results are electronically available as supplemental material.

DOI: 10.1103/PhysRevA.93.022704

I. INTRODUCTION

The energy loss of charged particles in matter has been addressed for over 100 years in fundamental and applied nuclear physics research. A century of extensive investigation has passed, but a new demand on accurate stopping power data is being pushed by modern technological applications and sophisticated modeling tools: precise measurements are required in materials science and engineering [1–4], medical physics [5], ion implantation and modification of materials [6], and also in all ion beam analysis (IBA) techniques [7–11], being a mandatory prerequisite for precise validation of theoretical models [12].

IBA is among the few techniques capable of measuring elemental composition in materials with high precision, nondestructively, in a model-independent approach and generally without the need of certified samples [13]. In the special case of self-consistent IBA [14], where several ion beam techniques are used on the same sample, various spectra are processed and simulated simultaneously and the description with the highest chance to be correct (determined by maximization of the likelihood function including all spectra) is elected to represent the sample [15]. The accuracy of the fundamental parameters used to simulate the spectra is critical to yield the convergence of the fit. As a matter of fact, the work of intercomparison of seven depth profiling IBA codes, sponsored by the International Atomic Energy Agency (IAEA) [16], has demonstrated that the most important factor affecting spectral shape is the absolute value of the stopping powers and cross sections used as input in those codes: this has also motivated the current need for accurate and traceable stopping power data. Accurate and traceable IBA is therefore undoubtedly dependent on better stopping powers and cross sections.

A comprehensive discussion about the importance of the uncertainty budget in IBA is given in the work by Sjoland *et al.* [17]: the analysis by only one IBA technique can easily be wrong when the budget of uncertainty is not taken in account or is missing. In fact, to achieve an accurate IBA (i.e., a quantification of the elemental composition of the sample with an error around 1%), the required experimental data on stopping powers need to be equally accurate and must therefore be retrieved from reliable databases, incorporating a correct treatment of the main sources of uncertainties. As a practical example, Jeynes *et al.* [18] and Colaux *et al.* [19] recently demonstrated the capability of a sample quantification from an RBS spectra with ∼1% of overall uncertainty, taking full advantage of the precision of the stopping power of protons in silicon (0.8% for 1.5 MeV proton energy [19], a rather exceptional case). Unfortunately, several common practices reporting measured stopping powers go against such needs. For example, experimental results quote errors that are not substantiated by a discussion on the budget of uncertainties and its traceability, or are given only in plots and not in a tabular form, or, last but not least, are given as a deviation relative to some specific theoretical model. Here we resist to all these habits.

Another growing application that requires a precise evaluation of stopping powers is cancer therapy using proton or other ion beams. Due to the fact that most tumors are commonly localized in the interior of the patient's body and because the rate of energy loss of protons and ions present a maximum close to the end of their penetration path (the Bragg peak), the use of these beams is becoming a prominent technique in the treatment of deep tumors by maximizing the energy deposition at a proper depth, consequently reducing the damage on the surrounding healthy tissues. To achieve such a high level of control in the planning of the irradiation sessions, stopping powers are needed with high precision [20]. Several levels of difficulties in obtaining reliable and accurate stopping powers

*moro@if.usp.br; web.if.usp.br/gfaa

in organic tissues need to be overcome. No single strategy will succeed in mastering all difficulties and we see two main routes approaching the problem. The first is the most obvious one: directly measuring the stopping powers in biological samples. However, preparing suitable targets is difficult because of the heterogeneous nature of biological tissues, being neither solid nor liquid [21–23]. Limandri *et al.* [24] have recently reported the energy loss of H^+ and He^+ in hydroxyapatite films (a proxy for bones), providing experimental data with sufficient precision to verify in detail the validity of the additivity rules. The second route is to select monoelemental materials that can be prepared in thin films under well controlled conditions, to measure the stopping powers with high accuracy (here we present data for Al with an overall uncertainty of $<1\%$) and with very well quantified uncertainties to provide a stringent test of advanced theoretical models.

Concerning theoretical approaches, Paul *et al.* [25] argue that in spite of several efforts over the years to achieve a full description of the stopping powers, this has not yet been attained and for the specific case of low-energy beams, there are still unsolved disagreements between the theory and experimental results even for proton and α projectiles. For example, the most commonly used code for calculating the stopping power of protons and ions in materials, the Stopping and Ranges of Ions in Matter (SRIM) developed by Ziegler and collaborators over several decades [26,27], has an overall accuracy for all elements not better than $\sim$6.0% for proton and α beams. In a more recent work, Paul *et al.* [28] argue that below 30 MeV/u, SRIM is on average $\sim$6% higher than experimental results for heavy elements and $\sim$5% lower for light ones. Concerning modern computer simulation codes used to process IBA data, the problem is not much different. Mayer *et al.* [29] argue that the SRIM code did not undergo major improvements in its formalism (except by internal database updates) in its last versions. They also state that the uncertainty of the stopping powers is often the major source of uncertainties in the simulation of IBA spectra [29]. A comprehensive comparison of the codes (or the most advanced theories) most commonly used to calculate stopping powers against experimental results with thoroughly quantified uncertainties is a monumental work essentially never undertaken. Only partial benchmarks are scattered around several papers and we have no means to reverse the situation in the present work: we will only provide one more limited evaluation of some of the most widely used programs. Our lack of thoroughness is mitigated by the fact that the energy region of a few MeV covered here is particularly difficult for protons because it contains the transition from an intermediate-energy region, where the Varelas-Biersack parametrization is valid, to a high-energy one, where the Bethe-Bloch equation is appropriate.

The present paper aims at measuring the stopping cross sections of Al and Mo foils for protons in the energy range of 0.9–3.6 MeV with high accuracy, employing a rigorous experimental protocol using the transmission method. An extensive and traceable determination of the errors affecting the results was undertaken. We selected Al and Mo foils as targets. The stopping power of protons in the former has been covered by several independent publications [30] and can be used to benchmark our method and the way we estimate our uncertainties. The stopping power of the latter is essentially unmeasured in the energy range covered: there are only a few data points for Mo in the same database [30]. The choice of Al and Mo also aims at covering one low-Z and one medium-Z case to test the theoretical models. This paper is structured as follows. The experimental method is described in Sec. II, the results are presented in Sec. III, the comparison with theoretical models is shown in Sec. IV, and our final conclusions are drawn in Sec. V. In particular, the advantages of using the transmission method are pointed out in Sec. II A, and the beam energy calibration and all the necessary corrections, including the pulse height defect (PHD), are discussed in Secs. II B and II C, respectively. The effects of the PHD in the energy loss measurements are discussed in Sec. II D. The excellent energy stability of our tandem accelerator enabling precise measurements is demonstrated in Sec. II B. We pay special attention to fully characterizing our samples: we experimentally determine their impurities and correct our results using the Bragg rule and also devise a clever method to correct for local nonuniformities of the foil thickness; see Secs. II E and II F, respectively. The results for Al and Mo are compared with 131 and 46 other experimental data from literature, respectively, in Sec. III A and the budget of uncertainties is detailed in Sec. III B. To compare our data, we use the Varelas-Biersak parametrization to subtract the common gross behavior; the determination of its parameters is presented in Sec. III C. A complete comparison to the calculated stopping cross sections using the most widely adopted programs (SRIM 1985, SRIM 2013, PSTAR, CASP 5.2) and the Monte Carlo codes from the GEANT series (GEANT 3 and GEANT 4) is given in Secs. IV A and IV B, respectively. Finally, to contribute to the international stopping cross sections database, we present our data in tabular form in the Supplemental Material [31].

II. EXPERIMENTAL PROCEDURE

A. Transmission method

The transmission method [32,33] was used to measure the energy loss of protons in the absorber foils and to obtain the stopping cross section data. A primary proton beam collimated to 1.8 mm diameter and with typical beam current of $\sim$10.0 nA was first directed onto a very thin gold foil with 94.3 ± 0.9 μg/cm^2 areal density. The vacuum pressure in the scattering chamber was kept at $(5 \pm 1) \times 10^{-6}$ Torr at all time. The Au-backscattered protons were collected on a passive implanted planar silicon (PIPS) detector located at a scattering angle of $(120.0 \pm 0.5)^\circ$ as shown in the diagram in Fig. 1(a). The absorber foil was placed close to the detector in such a way that approximately half of the detector active area was exposed directly to the Au-backscattered particles while the other half, covered by the absorber foil, measured the protons after passing the foil and losing part of their energy; see Fig. 1(b). Due to the size of the slit, the scattering angle can change at most by $\sim 0.1^\circ$; this value is smaller than the uncertainty associated with the detector position ($\pm 0.50^\circ$).

The transmission method produces two peaks in the same energy spectrum: one of the Au-backscattered protons, and the other at a lower energy, due to protons that passed through the

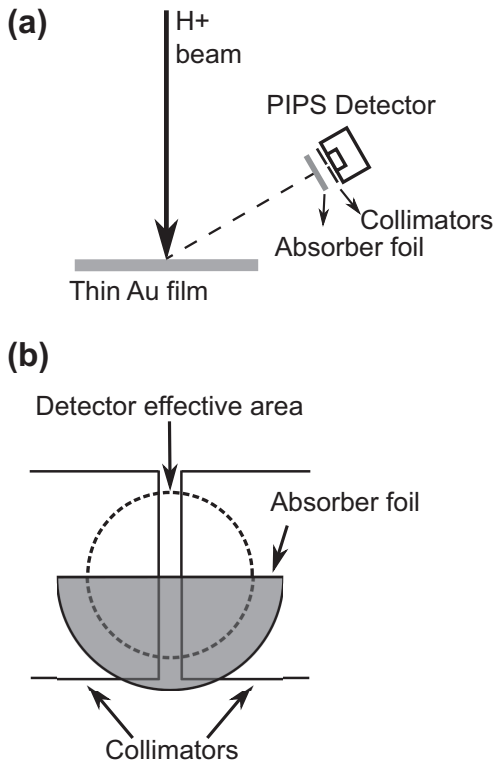

FIG. 1. Schematic diagram of the experimental setup. (a) Relative positioning of the Au scattering foil, absorber foil, and PIPS detector. (b) Absorber foil in front of the PIPS detector.

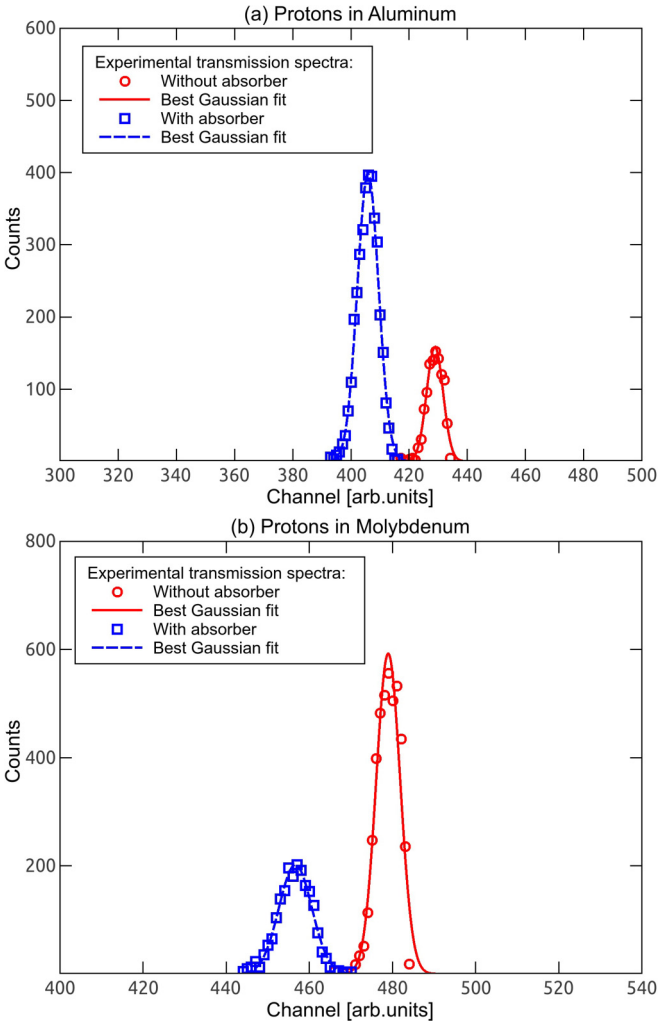

FIG. 2. Typical transmission spectra for Au-backscattered protons partially stopped in Al (top) and in Mo (bottom) foils. The energy difference of the peaks is related to the stopping power of the Au-scattered protons in the foils (see text). The peak height difference is due to variations in the position of the absorber foils in front of PIPS [see Fig. 1(b)].

absorber foil. An example of typical transmission spectra is shown in Fig. 2. Both peaks were fitted using a Gaussian profile [34–37]. The energy difference of the centroids was used to determine the energy loss of the protons passing through the foil. In the energy spectra shown in Fig. 2(a), the energy of the Au-backscattered protons is $E_1' = 2612.8 \pm 2.6$ keV and the measured energy difference between the primary and the Al-transmitted peak is $\Delta E' = 142.21 \pm 0.68$ keV. In Fig. 2(b), the energy of the Au-backscattered protons is $E_1' = 2908.9 \pm 2.8$ keV and the energy difference between the primary and the Mo-attenuated peak is $\Delta E' = 133.1 \pm 1.1$ keV. To get the nominal energy loss ΔE from the measured $\Delta E'$, it is necessary to correct for the electronic gain of the data acquisition system and the nonlinear response of the detector (e.g., dead-layer and nonionization processes; see Sec. II C). The different peak heights in Fig. 2 are due to variations in the position of the absorber foils, affecting the ratio of covered-to-uncovered detector areas in both data sets.

The advantages of the transmission method, here employed, can be summarized as follows: (i) the direct Au-scattered proton peak was used to precisely calibrate the electronics and as a reference to determine the energy loss in the absorber foil in each spectrum; this reduces the experimental uncertainty since the offset in the energy calibration cancels out (see Sec. II C); (ii) the position of the direct Au-scattered peak can be used to continuously monitor, and eventually correct, any fluctuation of the beam energy or of the electronics; (iii) the stopping cross section is better determined because it depends only on the difference of two PHD corrections at the two detected energies; (iv) the stopping power is less influenced by plural and/or multiple scattering, at least in the energy range considered here [32]; and finally, (v) because of the simplicity of the equations, tracking the uncertainties in the transmission method is simpler than in the case of a typical backscattering experiment.

B. Energy calibration

The measurements were carried out using the NEC-5SDH tandem accelerator of the Laboratory of Material Analysis by Ion Beams (LAMFI) of the Institute of Physics of the University of São Paulo. The beam energy E_0 was measured by the generating voltmeter (GVM) of the accelerator. The terminal voltage read by the GVM, V_{GVM}, was calibrated using several elastic backscattering (EBS) resonant reactions [38], combining different beams, energies, and targets, as presented in Table I. Since EBS resonant spectra are very sensitive to the projectile energy [13,15], the true beam energy has to be

TABLE I. Nuclear reactions used in the energy calibration of the GVM. The energy values at the resonance were retrieved from SIGMACALC [40].

Reaction	Energy (MeV)	Beam	V_{actual} (MV)
Si(p,p)Si	1.670	H^+	0.825
Si(p,p)Si	2.095	H^+	1.038
C(p,p)C	1.734	H^+	0.857
O(α,α)O	3.038	He^+	1.509
C(α,α)C	4.258	He^{2+}	1.413

determined with an appropriate procedure [39]. The accuracy of the outcome depends critically on the quality of the reference cross sections [14]. To avoid judging published resonant reaction data, and following a recommendation of Gurbich *et al.* [40] and Colaux *et al.* [39], we used the cross sections evaluated by SIGMACALC [40], which relies on well established nuclear reaction models fitted on selected experimental cross sections. This procedure provided calibration points all over the energy range utilized in the present investigation, but may have introduced an overall nonstatistical deviation (systematic error) if SIGMACALC values are found to be in error.

The GVM reading V_{GVM} and the actual terminal voltage V_{actual}, in MV, are linearly related by the following calibration function,

$$V_{\text{actual}} = a\, V_{\text{GVM}} + b,$$
$$E_0 = 2\, V_{\text{actual}} + E_{\text{inj}}, \tag{1}$$

where E_{inj} is the injection energy from the bias power supply of the primary ion source. E_{inj} was previously checked and determined at 20.00 ± 0.15 keV. The calibration parameters were $a = 0.982440 \pm 0.00061$ and $b = 0.01931 \pm 0.00067$ MV. The precision of this procedure was checked by successive repetitions yielding a standard deviation of ~0.1% for all proton beam energies employed in this work.

The GVM stability was determined recording the GVM values for each measurement. A typical example can be seen in Fig. 3. The mean standard deviation, in all sets of runs, was ~0.06%. Thus, the mean final uncertainty in the incident beam energy was 2.5 keV for both Al and Mo stopping cross section measurements.

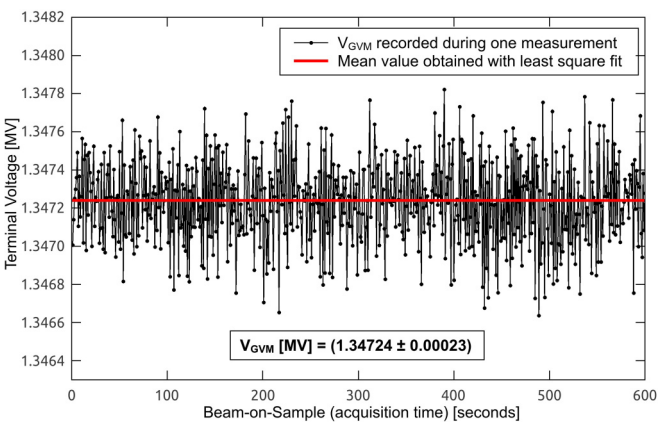

FIG. 3. Record of the terminal voltage, V_{GVM}, during one measurement of protons in aluminum.

C. Detector calibration and PHD correction

The nonlinearity of the energy-to-charge conversion of a PIPS detector has three main sources: (i) the energy loss in the passive entrance layer, (ii) the existence of energy loss mechanisms that do not lead to the formation of electron-vacancy pairs, and (iii) the incomplete collection of the generated charge. The sum of all these contributions is called the pulse height defect (PHD) [41,42]. For protons in the energy range of the present measurements, (i) and (ii) are the most relevant. The energy loss in the dead layer ΔE_{DL} of the detector is the largest contribution to the PHD under typical IBA conditions. This quantity is directly related to the dead-layer thickness X_{DL} and should be determined independently. In the present work, X_{DL} was measured previously, following the procedure described elsewhere [42], and was found to be ~450 TFU silicon equivalent (TFU is the acronym for thin-film units and it is equivalent to 10^{15} atoms/cm^2). The second most important contribution to the PHD is the small fraction of the proton energy ΔE_{NI} that is lost through nuclear collisions to processes that do not lead to the formation of electron-vacancy pairs (mostly phonon excitations [41]). In general the evaluation of this correction is complicated because secondary recoils can still produce electron-vacancy pairs and the full recoil cascade must be taken into account. Here we followed the approach described in Ref. [42] setting

$$\Delta E_{\text{NI}} = \eta \int_0^{E_i - \Delta E_{\text{DL}}} \frac{S_{\text{n,det}}(E)}{S_{\text{det}}(E)}\, dE, \tag{2}$$

where E_i, E, $S_{\text{n,det}}(E)$, and $S_{\text{det}}(E)$ are the proton initial kinetic energy, the proton kinetic energy during the slowing down, the proton nuclear stopping power, and the proton total stopping power, respectively. Obviously, $S_{\text{n,det}}(E)$ and $S_{\text{det}}(E)$ must be evaluated for the detector material (in our case, silicon). Finally, η, also known as the Lindhard partition function, represents the fraction of the energy of the recoiling silicon ions that does not lead to electron-vacancy pairs during the development of the full recoil cascade. Following Ref. [42], we assumed that η does not depend on the proton energy but only on the combination of the impinging ion atomic mass number and the detector material, and we took the parametrization from the same work (see Eq. (4) of Ref. [42]). For the nuclear and the total stopping powers of silicon, we adopted the SRIM 2013 values. The correction ΔE_{NI} was evaluated numerically for each energy of the Au-scattered protons and Al-attenuated or Mo-attenuated protons.

Once the PHD was known, the precise channel-to-energy conversion gain was determined using a proton beam scattered by the thin gold foil. The Au-scattered protons were detected at 120°. For each beam energy E_1, the center channel of the Au-scattered peak was determined by a Gaussian fit and plotted against its measured energy, corrected for the PHD, E_1'. The Au film was thin enough to make the detector resolution the main peak broadening effect. The calibration parameters G and O were determined fitting the equation

$$E_1' = E_1 - \Delta E_{\text{PHD}}(E_1) = G\,\mathcal{C} + O. \tag{3}$$

To compensate for any possible time drift of the electronics, this procedure was repeated every day on which we took experimental data and the corresponding G and O were always employed accordingly. To give a quantitative feeling of the achieved precision for 25 different proton energies ranging from 1.0 MeV to 3.4 MeV the G value yielded 5.9474 ± 0.0043 keV/channel.

D. Energy loss measurement

For the transmission spectra shown in Fig. 2, the nominal energy difference ΔE between the Au-backscattered protons and the Al-attenuated protons was obtained taking the distance between the centroids of the two peaks $\Delta E'$ and correcting them for the respective PHDs, by applying Eq. (3) twice, once to the impinging proton without absorber (nominal energy E_1 and measured energy E_1') and once to the proton after crossing the absorber (nominal energy E_2 and measured energy E_2'):

$$\begin{aligned} E_1 &= E_1' + \Delta E_{\mathrm{PHD}}(E_1), \\ E_2 &= E_2' + \Delta E_{\mathrm{PHD}}(E_2) \approx E_2' + \Delta E_{\mathrm{PHD}}(E_2'). \end{aligned} \tag{4}$$

The last approximation in Eq. (4) avoids solving numerically the implicit equation to obtain E_2 from E_2', and is a very good approximation at present experimental conditions. The true ΔE can be expressed in terms of the channel difference $\Delta \mathcal{C}$ of the centroids of the two peaks

$$\begin{aligned} \Delta E &\approx G\,\Delta \mathcal{C} + \Delta E_{\mathrm{PHD}}(E_1) - \Delta E_{\mathrm{PHD}}(E_2') \\ &= G\,\Delta \mathcal{C} + [S(E_1) - S(E_2')] X_{DL} \\ &\quad + [\Delta E_{\mathrm{NI}}(E_1) - \Delta E_{\mathrm{NI}}(E_2')], \end{aligned} \tag{5}$$

where $S(E_1)$ and $S(E_2')$ are the silicon stopping powers at the energies E_1 and E_2', respectively, X_{DL} is the dead-layer thickness, and $\Delta E_{\mathrm{NI}}(E_1)$ and $\Delta E_{\mathrm{NI}}(E_2')$ are the corrections for the nonionizing energy losses at energies E_1 and E_2', respectively. By measuring simultaneously both peaks with the same detector and the same electronics, the O parameter cancels out in Eq. (5), increasing the accuracy of the results. Furthermore, only the differences in the stopping powers and the nonionizing energy loss corrections, which are small, appear in Eq. (5), further reducing the impact of any inaccuracy in their evaluation. To give a quantitative feeling, the PHD overall value is ~0.10 keV and ~0.095 keV for the proton energies used for the Al and Mo stopping power measurements, respectively, accounting for a correction of the stopping cross sections by 0.086% and 0.081%, respectively, as shown in Table III. By measuring the two peaks at the same experimental conditions, the transmission method benefits from the cancellation of the O parameter and the small contribution of the difference in the PHD correction, since both peaks are reasonably close in energy.

E. Foil thickness and impurities

The thicknesses of the absorber foils were determined by measuring the mass-area ratio. The mass was obtained by a high-precision scale (Sartorius balance, model SE2), with nominal certified accuracy of 100 ng (readability). The scale was recalibrated with 10.000 ± 0.001 mg standard weight before use. The area measurement was done optically using a 15-MP professional camera positioned 1 m away from the foils to avoid parallax effects. The areas of the foils were determined from measurements obtained by processing 10 different pictures with IMAGEJ software [43]. The thicknesses were found to be 1.5305 ± 0.0038 mg/cm^2 and 2.425 ± 0.012 mg/cm^2 for Al and Mo, respectively.

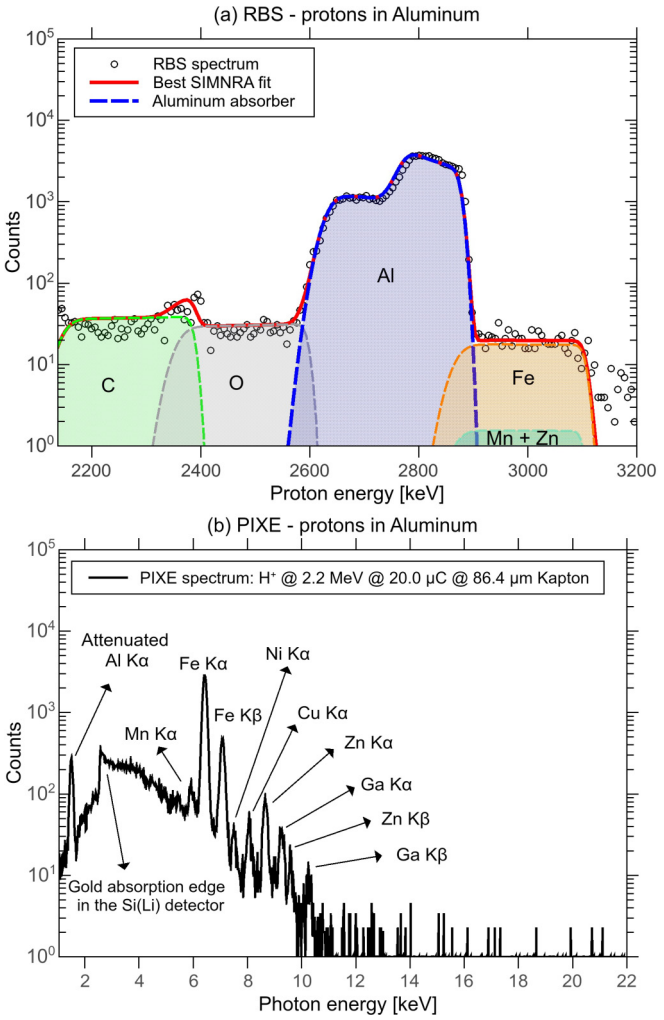

FIG. 4. Example of RBS (a) and PIXE (b) spectra of the aluminum foil. The impurity levels were obtained from these techniques with self-consistent analysis.

The contaminants in both absorbers were quantified using Rutherford backscattering spectrometry (RBS) and particle-induced x-ray emission (PIXE) techniques, both in a low-current and high-integration-time regime. With RBS, it was possible to quantify the light contaminants (essentially C and O) in both foils, and the conditions for these measurements were 5.0 ± 0.5 nA current and 3.4 MeV proton beam integrated to 8.0 ± 0.4 μC and 16.0 ± 0.8 μC for Al and Mo, respectively. The backscattered protons were detected using a PIPS detector with a resolution of the 17-keV FWHM positioned at 120°. A typical RBS spectrum for Al is shown in Fig. 4(a). With PIXE, it was possible to quantify the heavy elements ($Z > 13$) in both foils, and the conditions for these measurements were 1.0 ± 0.1 nA current and 2.2 MeV proton beam integrated up to 20.0 ± 0.2 μC and 10.0 ± 0.1 μC

for the Al and Mo foils, respectively. The characteristic x rays were detected with a Si(Li) detector (144 eV FWHM at Mn $K\alpha$) positioned at 90°. To enhance the detection of high-Z and low-level impurities a Kapton filter with 86.4 ± 0.1 μm thickness was placed in front of the x-ray detector. According to XCOM [44], the attenuation factors for the Al $K\alpha$ and Mo $L\alpha$ characteristic lines are $\sim 1.4 \times 10^{-5}$ and ~0.21, respectively. A typical PIXE spectrum, of the Al foil, is shown in Fig. 4(b). As a side note, the Kapton filter enabled the collection of a spectrum with high statistics without overloading the detector, which made the absorption edge of the Si(Li) gold contact clearly visible in Fig. 4(b).

The RBS data were fitted using MULTISIMNRA software [45,46] and adopting the SRIM 2013 stopping powers. SIGMACALC cross sections were used for C and O elements, and the cross-section data by Chiari *et al.* [47] were assumed for Al, in the absence of SIGMACALC cross sections for this combination of element and beam energy. For the other elements, the cross sections were supposed to be Rutherford-like. For the Al foil the impurity concentrations were C (0.986 ± 0.064)% and O (0.687 ± 0.058)%. The Fe, Mn, and Zn contaminations in the RBS spectrum are overlapped; hence a combined RBS and PIXE analysis was used to quantify Fe (0.13013 ± 0.0041)%, Mn (0.0341 ± 0.0010)%, and Zn (0.0098 ± 0.0021)%. The remaining elements (Ni, Cu, and Ga) account for less than 0.001% of the Al foil, with a negligible effect in the measurement of its stopping power. The measured Al foil purity is 98.2 ± 6.7 at. %. Using a similar approach for the Mo foil, the impurities identified by RBS were C (1.86 ± 0.45)% and O (0.82 ± 0.19)%. The only impurity identified by PIXE was a small concentration of Fe (0.00641 ± 0.00024)%. The other remaining elements (Ni, Cu, and Ga) account for less than 0.001% of the Mo foil, and again the change in the Mo stopping power was therefore negligible. The measured Mo foil purity is 97.3 ± 18.4 at. %.

To calculate the effect of the impurities in the foils, we used the Bragg rule assuming SRIM 2013 stopping powers for the contaminants [48]. That correction affected the final stopping powers of Al and Mo by 0.000017% and 0.0010%, respectively. Supposing an uncertainty of 5% in the SRIM 2013 data [28], the contaminants account for an uncertainty in the final stopping power of 0.000080% for Al and 0.00011% for Mo. Though negligible, the contribution of this correction and its uncertainty was included in the final uncertainty budget in Table III.

F. Foil thickness nonuniformity

Since the aim of the present work is to determine stopping cross sections with high accuracy, we found that the foil thickness nonuniformity, hardly considered in other works, is rather important. The method here adopted to experimentally correct for the nonuniformity is based on three steps: (a) for each absorber, three sets of stopping cross sections were measured in three different regions of the foil (i.e., the position of the foil was slightly shifted relative to the PIPS detector), (b) the Varelas-Biersack model for the stopping cross section was fitted to all three sets of data, assuming the nominal (measured) target thickness, determining the free parameters A_1, A_2, A_3, and A_4 (see Sec. III C), and (c) a free multiplicative parameter

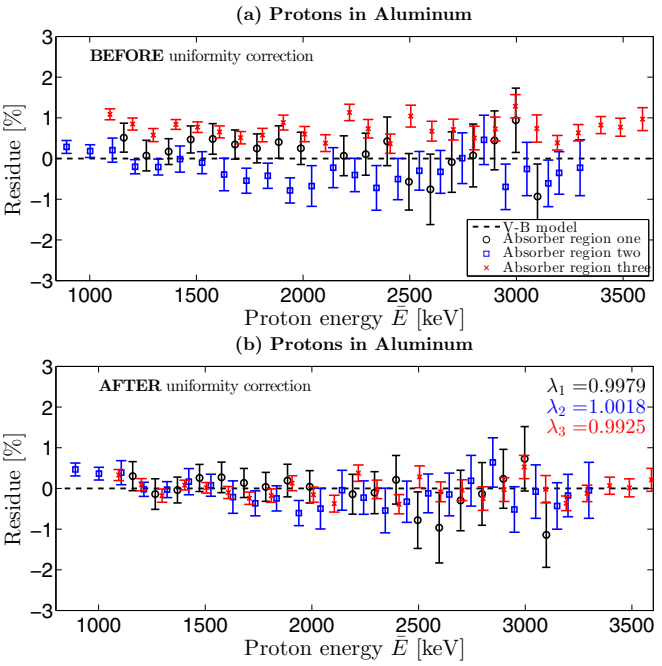

FIG. 5. Example of the nonuniformity correction of the Al foil. The three sets of stopping powers measured in three different regions of the target are shown in (a). The same three sets of data are displayed again in (b) after correcting for the foil thickness nonuniformity.

λ_i was applied to the target thickness of each set, searching the best λ_i that minimizes the square difference of the ith set keeping the previously determined values of A_1, A_2, A_3, and A_4 fixed. A quantitative estimate of the foil thickness variability is given by $\Delta\lambda = \frac{1}{2}(\max \lambda_i - \min \lambda_i)$. We found $\Delta\lambda = 0.46\%$ and 1.3% for Al and Mo, respectively. These nonuniformities are equivalent to ~27 nm and ~31 nm for Al and Mo, respectively. The procedure is illustrated in Fig. 5 for the Al foil. In Fig. 5(a) the three sets of slightly displaced points, corresponding to the three different regions of the target, can be clearly identified by eye. In Fig. 5(b), after the correction, they all merge into a single cloud without any visible systematic trend.

III. RESULTS AND DISCUSSION

A. Experimental results

The main results of the present paper are the experimental stopping cross sections S of Al and Mo for protons in the energy range of 0.9–3.6 MeV measured in steps of ~50 keV. The data are shown in Figs. 6(a) and 6(b), with their corresponding uncertainties. They were obtained by the ratio between ΔE from Eq. (5) and $\lambda_i \, \Delta x$ determined as described in Secs. II E and II F. In the transmission method, the target average stopping cross section S is attributed to the mean energy $\bar{E}$:

$$\bar{E} = E_1 - \frac{\Delta E}{2}, \quad S = \frac{\Delta E}{\lambda_i \, \Delta x}, \tag{6}$$

where the symbols have the same meaning as in Sec. II C. These equations are better than 0.05%, whenever $\Delta E / E_1 \lesssim$

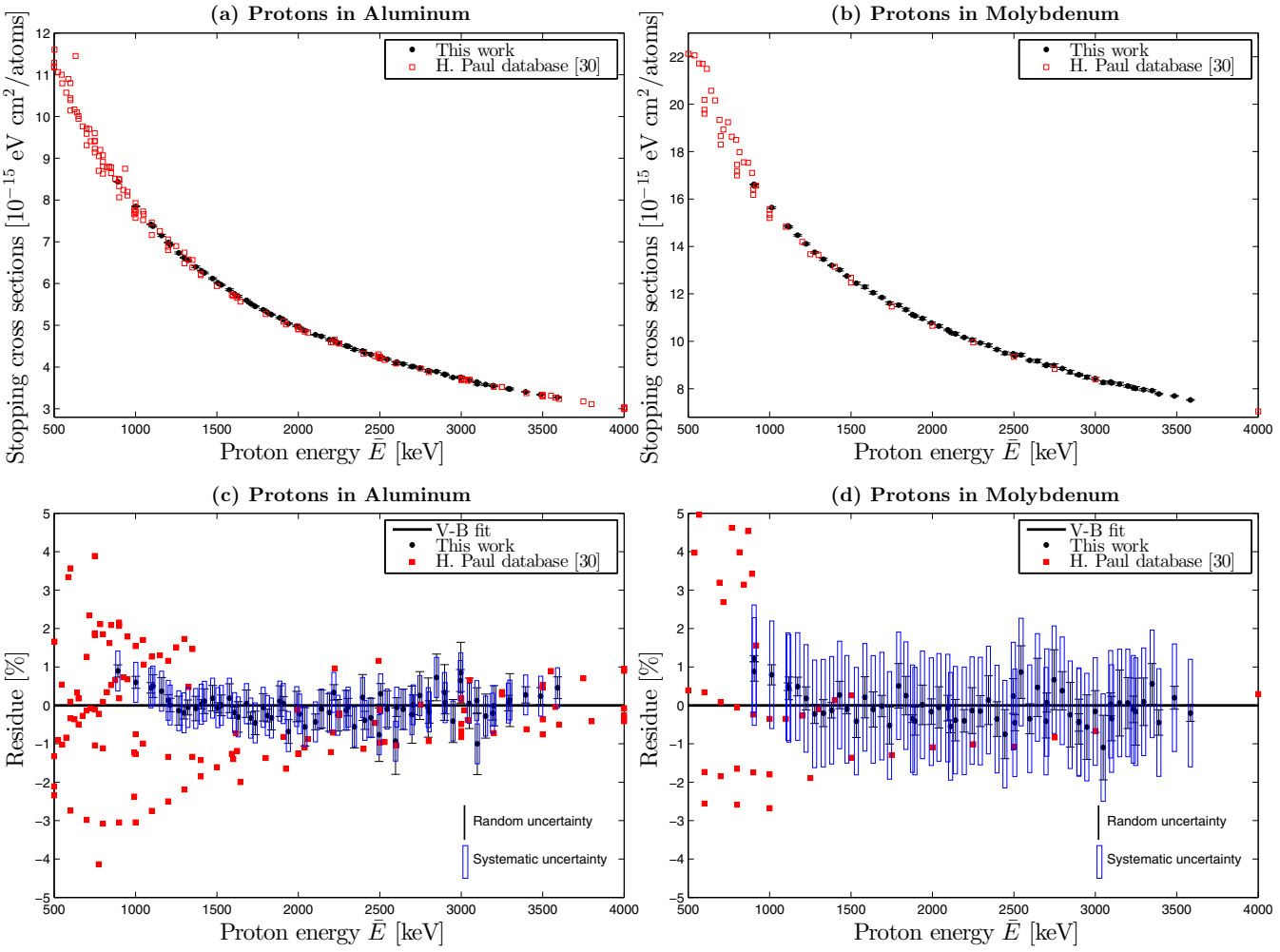

FIG. 6. Experimental stopping cross sections (solid circles) for Al (top left) and for Mo (top right) compared with all the other data (squares) of the Paul database [30]. The lower panels show the deviation of the same data to the VB model (see text for details). The vertical bars and the vertical rectangles represent the random and systematic uncertainties, respectively.

20% [35,49], which applies to all measurements here presented.

The upper energy limit on the $\bar{E}$ is imposed by the maximum terminal voltage of the tandem accelerator. The lower energy limit is set by the requirement $\Delta E/E_1 \lesssim 20\%$. When this condition is violated, the corresponding energy distribution is not Gaussian compromising the determination of both ΔE and $\bar{E}$. Moreover, the energy of the secondary Au-scattered beam particles can depend significantly on the depth of interaction in the Au foil. The use of a self-supporting Au foil dictated a practical minimum thickness for the present measurements, setting a minimum energy limit E_0 of ~950 keV, equivalent to a low energy limit of the diffused protons $\bar{E} \sim 890$ keV for Al and Mo. Because for $\bar{E} \sim 890$ keV, $\Delta E/E_1 \sim 20\%$, both conditions actually coincide.

The results are compared with other published data in Figs. 6(a) and 6(b) for Al and Mo, respectively. To avoid rescanning and classifying the huge database of published Al and Mo stopping cross sections, we used the data in Paul's compilation [30]. In this compilation, more than 25 years of collected data, classified according to projectile and target species, are freely available in electronic form together with their uncertainties. For Al and Mo, the database contains 131 and 46 data points, respectively; however for the Mo, only 20 fall within the energy range studied in the present work.

To investigate in more detail the consistency of the measured data, their common gross behavior has been subtracted using the Varelas-Biersack parametrization (VB parametrization; see Sec. III C) making even small deviations clearly apparent [see Figs. 6(c) and 6(d)]. The semiempirical parameters of the VB parametrization were determined fitting all data together in the energy range from 0.5 keV to 4.0 MeV, abandoning the common practice of limiting the validity of the VB parametrization to below ~1 MeV [50]. The advantage of employing the VB parametrization is its simplicity and its smoothness rather than its absolute accuracy. Other more accurate expressions are available (see Sec. IV A) but unfortunately they exhibit discontinuities in the energy region here considered.

Because Al stopping powers are well known from several independent publications, they also served to validate the present implementation of the transmission method. Indeed, there is a very good agreement of our data with published ones

TABLE II. Budget of the main sources of uncertainty affecting the stopping cross section for the measurements shown in Fig. 2. The impact on S has been found by changing the corresponding parameter alone by its estimated error and propagating this variation. The classification of each contribution according to its type, A or B (second column), follows the definition described in Ref. [51] and the nature of its influence on S (last column) is also provided.

Parameter	Type	Parameter value		Parameter uncertainty		Unit	Effect on S (%)		Influence on S
		Al	Mo	Al	Mo		Al	Mo	
Beam energy	A	2612.8	2908.9	2.6	2.8	keV	0.042	0.041	random
ΔChannel	A	23.9109	22.3371	0.0064	0.0089	channels	0.14	0.35	random
Pulse high defect (ΔE_{PHD})	B	0.027	0.015	0.027	0.015	keV	0.019	0.011	systematic
Electronic calibration (G)	A	5.9498	5.9603	0.0043	0.0042	keV/channel	0.073	0.071	systematic
ΔE [see Eq. (5)]	A	286.47	253.37	0.45	0.62	keV	0.48	0.83	random
Target thickness	A	34186	15229	86	77	10^{15} atoms/cm^2	0.25	0.51	systematic
Target impurities	A	632	410	30	74	10^{15} atoms/cm^2	0.0012	0.0036	systematic
Target nonuniformity	A			27	31	nm	0.46	1.3	systematic
Stopping power of impurities	B	26.5	11.41	1.3	0.58	10^{-15} eV cm^2/atom	0.068	0.037	systematic
Scattering angle (kinematic)	B	120.00	120.00	0.50	0.50	degrees	0.0079	0.078	systematic
Random uncertainty for only this measurement							0.48	0.82	
Systematic uncertainty for only this measurement							0.53	1.4	
Total standard error (summed in quadrature) for only this measurement							0.87	1.4	

as shown in Fig. 6(c), where we also display the estimated random and systematic uncertainties. The uncertainties of other measurements are often not quoted or not separated into random and systematic, and for this reason it was decided to represent only the data points. It is generally observed that measurements from different authors tend to scatter dramatically in the region around the Bragg peak (see Fig. 6). However, most of them fall within the error bars of the present set. For the Mo case, there is also a nice agreement between our data and others above ∼1 MeV, where the difference between the different authors is smaller.

B. Uncertainty budget

The quantitative analysis of the various contributions affecting the stopping power measurements is usually not given in the literature. Our goal in the following discussion is to provide a rigorous evaluation of the sources of uncertainty in the present measurements, demonstrating an unbroken chain of measurements and associated uncertainties ending in a calibrated standard or in a widely accepted physical reference quantity (e.g., in the case of the energy calibration using the non-Rutherford resonant cross sections). This procedure is known as traceability. These calculations were made varying

TABLE III. Budget of the main sources of uncertainty affecting the stopping cross section. The impact on S has been calculated as in Table II. The averages over all the measurements are shown separately for Al and Mo. The classification of each contribution according to its type and its influence on S is the same as in Table II.

Parameter	Type	Parameter uncertainty averaged over all data		Unit	Effect averaged over all S data (%)		Influence on S
		Al	Mo		Al	Mo	
Beam energy	A	2.5	2.5	keV	0.044	0.040	random
ΔChannel	A	0.0089	0.0098	channels	0.087	0.076	random
Pulse high defect (ΔE_{PHD})	B	0.0049	0.0048	keV	0.086	0.081	systematic
Electronic calibration (G)	A	0.0049	0.0048	keV/channel	0.077	0.081	systematic
ΔE [see Eq. (5)]	A	0.58	0.65	keV	0.28	0.29	random
Target thickness	A	86	77	10^{15} atoms/cm^2	0.25	0.51	systematic
Target impurities	A	30	74	10^{15} atoms/cm^2	0.0012	0.0037	systematic
Target nonuniformity	A	27	31	nm	0.46	1.3	systematic
Stopping power of impurities	B	1.3	0.58	10^{-15} eV cm^2/atom	0.068	0.037	systematic
Scattering angle (kinematic)	B	0.50	0.50	degrees	0.0079	0.078	systematic
Random uncertainty averaged over all measurements					0.32	0.44	
Systematic uncertainty for all measurements					0.54	1.4	
Total standard error (summed in quadrature) for all measurements					0.63	1.5	
Root mean square of all current data (in the residue plot of Fig. 6)					0.34	0.44	

each parameter separately (considering the sources uncorrelated) assuming its estimated uncertainty and determining how these changes affect the stopping cross section on average. As an example, we show in Table II the budget of uncertainties corresponding to the spectra shown in Fig. 2. In Table III, we report a summary of the uncertainty budget averaged over all measurements. The uncertainties displayed in these tables were classified as type A or B, following the definition of the Joint Committee for Guides in Metrology [51]. We also divided the effect of each source of uncertainty into random or systematic (last column). For example, the error in the determination of the positions of the peaks affects the stopping cross section in a random way (such an error affects independently each datum and cannot be corrected in the final result), while the error in the determination of the foil thickness affects systematically the whole set of data (and may in principle be corrected if the foil thickness would be better determined). The total contributions of these two kind of uncertainties are stated separately as error bars and error rectangles in Figs. 6(c) and 6(d).

At present experimental conditions, the major contribution to the systematic error in the stopping cross sections comes from the uncertainty in the determination of the foil thickness (including its nonuniformity). This is evidence that the major limitation of the transmission method, at least in the energy interval covered in the present work, is the quality of the foils. On the other hand, the major contribution to the random uncertainty in the stopping cross sections comes from the error in the determination of the peak position (including the Gaussian fit accuracy), which is related to the binning of the histogrammed spectrum [52]. It is worth pointing out that, once the counting statistics is enough to accurately determine the positions of the peaks, a precise measurement of the integrated charge is not required in the transmission method. For this reason the integrated charge is not mentioned in the uncertainty budget. The stopping cross sections results have a mean relative random uncertainty of 0.32% for Al and 0.44% for Mo, and a systematic uncertainty of 0.54% for Al and 1.4% for Mo (see Table III), firmly establishing the high accuracy of the present measurements.

The smooth VB parametrization used to fit the experimental data in Fig. 6 describes appropriately the common behavior of all data in the energy region of interest and is particularly useful in comparing small variations of all data and theoretical models. The estimate of the random uncertainties is confirmed by comparing it to the root mean square deviations of the residuals of the experimental points (see Table III). Indeed, the standard deviation of our data relative to the VB curve, of 0.34% and 0.44% for Al and Mo, respectively, is very close to the calculated random uncertainties of the 0.32% for Al and 0.44% for Mo (see Table III).

C. Evaluation of the Varelas-Biersack parametrization

The energy loss process has the peculiar feature of assuming different regimes according to the projectile kinetic energy E. For incident energies E of few keV, the stopping power is proportional to the projectile velocity, while for high energies, above a few MeV, the stopping power is well accounted for by the Bethe-Bloch formalism (see Sec. IV). The description of the transition from the low to the high energy regime is a difficult task and still an active field of research (see Sec. IV A). In 1970, Varelas and Biersack [53] introduced a semiempirical expression (here called the VB parametrization) to evaluate stopping power curves. Later, in 1977, Andersen and Ziegler [54] devised an improvement to the VB model that is especially good for an energy range from $E_{R0} \sim 10$ keV up to $E_{R1} \sim 1000$ keV. Their VB parametrization has the form

$$\begin{aligned} S_{VB} &= \frac{s_{low}\, s_{high}}{s_{low} + s_{high}}, \\ s_{low} &= A_1\, E_s^{0.45}, \\ s_{high} &= \frac{A_2}{E_s}\, \ln\left(1 + \frac{A_3}{E_s} + A_4\, E_s\right), \end{aligned} \tag{7}$$

where A_1, A_2, A_3, and A_4 are four semiempirical coefficients. The independent variable in the equations above, E_s, is the particle kinetic energy normalized to its mass (in atomic mass units). The parameters A_1, A_2, A_3, and A_4 are determined by fitting the equation to experimental data. The most recent compilation of generally accepted values for A_1, A_2, A_3, and A_4 is part of the ICRU 49 report [50]. For Al and Mo they agree numerically with those given in the original work by Andersen and Ziegler [54] (see Sec. IV A).

As mentioned previously, the most important feature of Eq. (7) is its ability to reproduce the gross behavior common to all experimental data in the region of interest, not its accuracy. For this reason, we used this equation to fit all measurements (i.e., ours and others [30]) in the energy range from 0.5 MeV up to 4.0 MeV. Equation (7) is nonlinear with respect to the coefficients, meaning that a nonlinear version of the least-squares minimization (χ^2) must be employed to fit this model. To obtain the particular set of coefficients for the VB model, that combines the present data with the previous ones, we considered three subsets of data in our fit. (i) The first subset contains the data presented in this work, with the stated uncertainties (random and systematic). (ii) The second subset contains experimental results from the literature, using the compilation by Paul [30] with the corresponding uncertainties, even though they are not divided into random and systematic. (iii) The third subset contains the previous knowledge of the coefficients presented in the ICRU 49, whose uncertainties are unknown.

The obtained VB coefficients ($A_1 = 5.20$, $A_2 = 2.84 \times 10^3$, $A_3 = 166$, and $A_4 = 1.76 \times 10^{-2}$ for Al and $A_1 = 6.33$, $A_2 = 9.52 \times 10^3$, $A_3 = 455$, and $A_4 = 4.81 \times 10^{-3}$ for Mo) were determined by a nonlinear least-squares method also including the systematic uncertainties of the data [51,55].

As can be seen in Fig. 6, the VB model with the new coefficients agrees well with our results for both Al and Mo. This fit will be used to subtract the common gross behavior of all data to aid the comparison with theoretical models in Secs. IV A and IV B. However, as Eq. (7) is a semiempirical description we will always show in addition our experimental data with error bars and error rectangles representing the random and systematic uncertainties, respectively.

IV. COMPARISON WITH THEORIES

A. Comparison with SRIM, PSTAR, and CASP

Theoretical descriptions of stopping powers can be divided into three main classes: (i) semiempirical approaches, (ii) simplified models, and (iii) full *ab initio* calculations.

A prototype of the first family has already been discussed in Sec. III C: theoretical studies are used as a guide to find a parametrization of the stopping power, like Eq. (7), that can describe reasonably well the data with relatively few free parameters, which are not calculated from first principles but rather determined by fitting energy loss measurements. SRIM [27] and PSTAR [56] (ICRU 49 [50]) have been selected for a comparison with the present results because of their widespread use. It is clear that calculations belonging to this class can never be better than the data that are used to determine their parameters: their quality is related to the expression used as much as to the care devoted in compiling and filtering the database of published values selected for fitting. Another feature is also obvious: the parameters are (or should be) frequently updated as more recent (and hopefully more accurate and reliable) measurements are made available. In this sense, it is not possible to state one definitive prediction, but only outcomes from some specific versions can be tested.

The second class is less well defined and rather broad. It contains theoretical approaches where approximations are made. Moreover, in some cases, not all of the quantities entering the calculations are obtained from first principles but are again determined from fitting the measurements. The main difference with the previous family of models is that these parameters have typically a well defined physical meaning. As an example, the reader can consider the Bethe-Bloch theory where the mean ionization potential I_{Bethe} is determined by adjusting experimental stopping powers [57]. The CASP [58] code belongs to such a category and it is among the few codes that are freely available and will be compared with the present data as well.

Finally, fully theoretical results, starting from atomic and solid state structure calculations, have been obtained in recent years. An example belonging to this family are the series of publications by Sigmund and Schinner who developed the binary stopping theory for swift heavy ions in matter [59–61]. One other approach that also deserves mentioning is the work of Montanari *et al.* [62] because it predicts, beyond the stopping power, the energy straggling parameter. However, the use of these methods is rather complex and is not common yet, partially because it has never been implemented in a freely available code. It remains beyond the scope of the present paper to compare our data with such type of prediction.

The most widely used program for calculating stopping powers is SRIM, developed over more than thirty years by Ziegler and several collaborators [26,27,54,63]. It belongs to family (i) and treats both protons, α particles, and heavy ions in essentially all targets and covering an energy range from 10 eV/u to 2 GeV/u. SRIM considers both electronic and nuclear stopping (which is important at low energies or for specific applications like damage evaluation and ion implantation in solids). However, in the case here presented, the electronic stopping dominates over the nuclear stopping power by at least three and two orders of magnitude for Al e Mo, respectively. The first version of SRIM from 1985 is fully open and the formula as well as the source code can be found in the book by Ziegler, Biersack, and Littmark [26]. Major improvements were undertaken in 1995, 1998, and 2003 [27,63]. In the 1985 version, the electronic stopping power of all ions is calculated by using the effective charge approach (treated with a parametrization inspired by the Brandt-Kitagawa theory [64]) to reduce it to the stopping power of protons in the same material and with the same velocity. The stopping power of protons is determined by a parametrization [26], similar to the Varelas-Biersack expression Eq. (7), fitted to the experimental data. The 1995 version added a more accurate description of the energy loss of protons above 10 MeV/u by adopting a Bethe-Bloch-like formula with shell-like corrections along the lines of the original Andersen-Ziegler approach [54]. The continuity between the two parts was ensured by appropriate constraints between their parameters. The shell-like corrections were implemented with a fourth-order polynomial in $\ln(E)$ where E is the proton kinetic energy. The change from a Varelas-Biersack-like expression to a Bethe-Bloch-like one was motivated by the incorrect high-energy behavior of the former (E^{-1}) when compared to the latter (β^{-2}). All free parameters were adjusted to experimental data and have been continuously improved from one version to the next. Ziegler compiled one of the best databases of published measurements (the list of the references before filtering is available [48]) and this is possibly one of the greatest strengths of SRIM. Unfortunately, the evolution of SRIM is hard to follow, because the code ceased to be open after 1995. A more detailed discussion about SRIM for low energies and heavy ions can be found in Ref. [65]; here the emphasis is on protons in the energy range relevant for IBA, but, as mentioned, the same parametrization works as a basis for heavy ions with the same velocity in the same target materials.

The stopping powers calculated with the first version of SRIM from 1985 and the most recent one from 2013 are tested against the present experimental data in Fig. 7. As in the lower panels of Fig. 6, the gross behavior of the data has been subtracted by using the VB parametrization Eq. (7) to enhance small deviations. For consistency with Sec. III C, the same values of the fitted parameters have been adopted. For Al, the changes from 1985 to 2013 have been less than for the Mo case: the newest version passes better through the present experimental points within the error bars [see Fig. 7(a) and 7(b)].

To compare the models with the experimental data (ours and others from [30]), we adopted a statical approach introduced by Paul and Schinner [66], who proposed to judge the reliability of a stopping power calculation using the variables

$$\Delta_{\mathrm{PS}} = \left(\left\langle \frac{S_{\mathrm{exp}}}{S_{\mathrm{calc}}} \right\rangle - 1\right) \times 100,$$
$$\sigma_{\mathrm{PS}} = \sqrt{\left\langle \left(\frac{S_{\mathrm{exp}}}{S_{\mathrm{calc}}}\right)^2 \right\rangle - \left\langle \frac{S_{\mathrm{exp}}}{S_{\mathrm{calc}}} \right\rangle^2} \times 100, \tag{8}$$

where $\langle\,\rangle$ indicates the average over the content of a stopping powers database and S_{exp} and S_{calc} are the measured and calculated stopping cross sections, respectively. The quantity Δ_{PS} is a normalized average deviation describing the

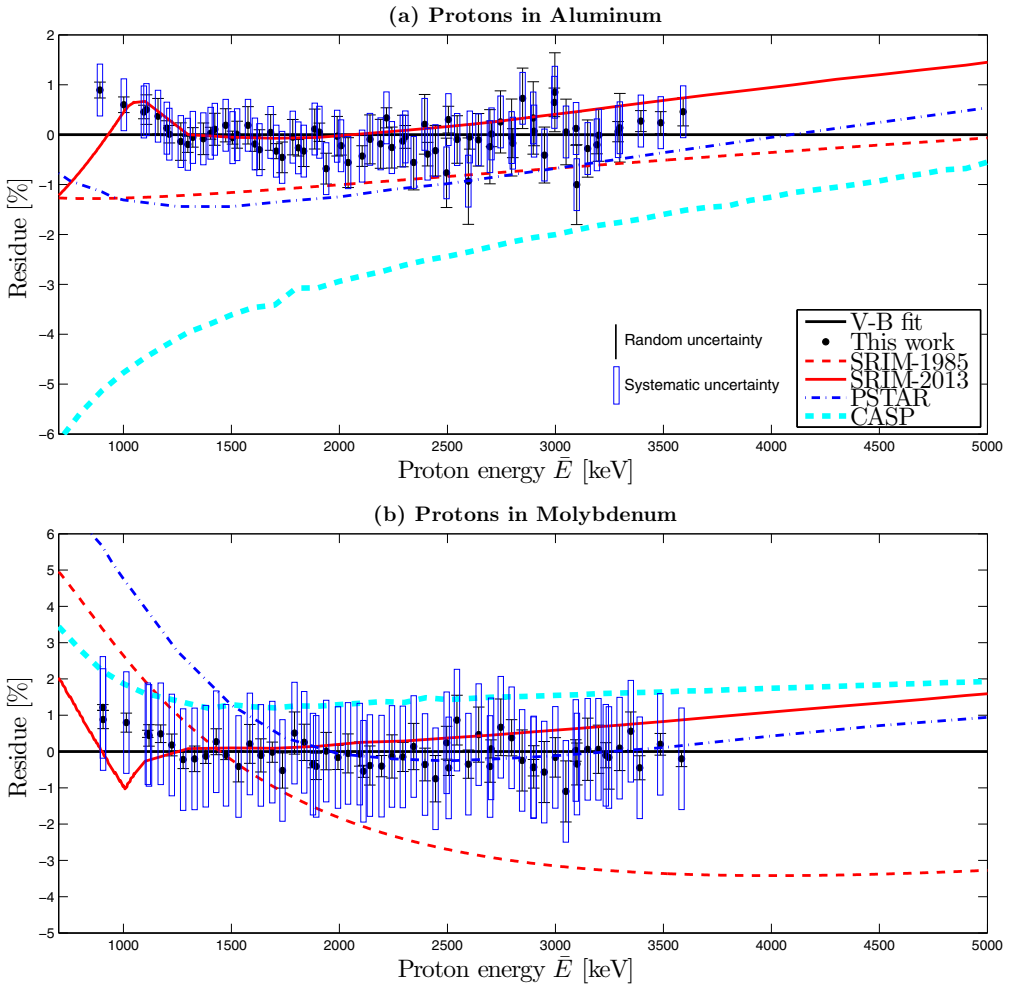

FIG. 7. Comparison between the present data (solid circles) and theoretical evaluations for Al and Mo [panels (a) and (b), respectively]. The same representation of the residuals from the VB parametrization Eq. (7), as in Fig. 6, has been adopted to show small deviations. The dashed line has been calculated with the 1985 version of SRIM (the first version of the software available by Ziegler *et al.*), the solid line with the latest version of SRIM (2013), the dash-dotted line with PSTAR, and finally the thick-dashed line with the newest version of the CASP code (5.2).

systematic difference between the calculation and the data, while σ_{PS} is a normalized root mean square deviation and provides information about the random fluctuation (i.e., the statistical error) of the measurements. Paul and Schinner [66] considered several theoretical models, including most of the ones discussed here, and found that SRIM 2003 (the newest version SRIM 2013 had not yet been released) is better than all other programs and its overall accuracy is ∼7.5% and ∼3.5% for solid elemental and for gaseous targets, respectively. The variables Δ_{PS} and σ_{PS} calculated for the present models with the present experimental points are given in Table IV.

The slightly better agreement of the new version of SRIM for Al (−0.22% versus 0.91%), as well as for Mo (−0.33% versus 1.7%) is apparent (the maximum deviation happens close to the lowest energies). As mentioned, the quality of semiempirical models depends on the adopted parametrization and how the free parameters are determined, i.e., on the quality of published data. The discrepancies between the 2013 version of SRIM and the present measurements are well within the 3.9% uncertainty margin for H^+ ions declared after the recent improvements (see Table 1 of Ref. [27]). Finally, the curve from the 2013 version exhibits a discontinuity in the derivative around ∼1 MeV, more pronounced for Mo than for Al. This was not the case in the 1985 version since Eq. (7) adopted at that time cannot show a discontinuity in the derivative. Because the details of the parametrization incorporated in the most recent improvements of SRIM have not been published, no further discussion is possible.

The ICRU 49 report [50], released in 1993, represents an attempt to reach a wide consensus on a semiempirical description of the stopping power of protons and α particles in matter with energies from 1 keV up to 10 GeV. Both electronic and nuclear stopping were considered, but as mentioned, in the energy range of current interest only the former is important and it is the only one that will be discussed here. The basic approach is still the same pioneered by Andersen and Ziegler in 1977 [54], with several improvements. Some of the models are common to the ICRU 37 report [67], a similar effort dealing with the stopping power of electrons. The kinetic energy range was divided into three regions: (i) a

TABLE IV. Quick comparison of the present experimental results with the theoretical calculations considered in Sec. IV A and the models implemented in the GEANT series described in Sec. IV B. The calculations or the simulations have been compared with the present data and separately with those from the database by Paul [30] using the variables Δ_{PS} and σ_{PS} introduced by Paul and Schinner [66]; see Eqs. (8).

	Present work $\Delta_{PS} \pm \sigma_{PS}$ (% ± %)		Other data [30] $\Delta_{PS} \pm \sigma_{PS}$ (% ± %)	
	Al	Mo	Al	Mo
SRIM 1985	0.91 ± 0.41	1.7 ± 1.7	0.72 ± 1.6	−0.82 ± 2.2
SRIM 2013	−0.22 ± 0.33	−0.33 ± 0.61	−0.51 ± 1.5	−0.71 ± 0.95
PSTAR	1.0 ± 0.43	−0.67 ± 1.3	0.81 ± 1.5	−2.8 ± 2.0
CASP 5.2	2.9 ± 1.1	−1.5 ± 0.39	3.1 ± 2.1	−2.2 ± 0.94
GEANT 3	−0.80 ± 0.33	−4.8 ± 0.45	−1.1 ± 1.5	−5.9 ± 1.0
GEANT 4–NIST	−0.67 ± 0.33	−4.1 ± 0.96	−1.0 ± 1.5	−5.6 ± 1.2
GEANT 4–USER	1.2 ± 0.47	−0.53 ± 1.3	0.89 ± 1.5	−2.7 ± 2.0

low-energy regime ($E < E_{R0}$) where the electronic stopping is proportional to velocity, (ii) an intermediate-energy region ($E_{R0} < E < E_{R1}$) where the improved VB parametrization, Eq. (7), is adopted, and finally (iii) a high-energy region ($E > E_{R2}$) treated with a modern Bethe-Bloch-type expression [57]. While the matching between regions (i) and (ii) is trivial because the low-energy limit of Eq. (7) already has the right behavior, joining parts (ii) and (iii) is more complex. The two regions have been separated by a reasonably wide gap ($E_{R1} < E < E_{R2}$) and a spline is used to interpolate in a Fano plot [i.e., $S\beta^2$ as a function of $\log(E)$]. The exact values of E_{R1} and E_{R2} have been selected by eye to give a smooth behavior (Al: $E_{R1} = 0.3$ MeV and $E_{R2} = 1.0$ MeV, and Mo: $E_{R1} = 0.75$ MeV and $E_{R2} = 2.0$ MeV). For Al and Mo, the parameters appearing in Eq. (7) given in the ICRU 49 [50] and in the work by Andersen-Ziegler [54] are the same.

For region (iii), the modern Bethe-Bloch expression includes (a) shell corrections, (b) the Bloch [68] and Barkas [69,70] corrections to the first-order Born approximation, and (c) the density effect correction [71,72]. Term (c) is important only for energies above several hundred MeV (and is not relevant here). The Bethe-Bloch formula is valid when the velocity of the projectile is much higher than that of electrons bound in the target atom; when this is not the case, term (a) must be taken into account [57]. The parametrization used for (a) is rather defying: the original ICRU 37 model was adopted in general, but a few elements were treated separately (Ag, Gd, W, Pt, Au, Pb and U). The parametrization of the original correction found by Bloch has been used for (b) as in the ICRU 37. The starting point to include the Barkas effect was the theoretical treatment given by Ashley, Ritchie, and Brandt [73–75]. However, for $Z \geqslant 64$ and $Z = 47$, the theory was replaced by the parametrization obtained by Bichsel [76] and was used to fit the experimental data. Detailed information can be found elsewhere [50]. The values of the mean ionization potential I_{Bethe} for each element are generally taken (with the exceptions of Ag, Gd, W, Pt, Au, Pb and U) from the ICRU 37 [67] and were themselves determined from data for protons and α particles. Indeed, I_{Bethe}, obtained as a fit to measurements, is not independent from how (a) and (b) are taken into account. More details on how the I_{Bethe} of the ICRU 37 was extracted can also be found in the paper by Seltzer and Berger [77].

Following all the refined procedures described in the ICRU 49 is itself a major effort; fortunately a table of stopping powers is provided at the end of the report. A complete implementation of the ICRU 49 recommendations has been done at NIST and embodied into the PSTAR code. This program is also accessible through a web interface on the NIST website [56] and has been used here.

Results from PSTAR have also been included in Fig. 7. For Al, there is an overall good agreement but a clear tendency to underestimate the present data below ∼1.5 MeV. For Mo, Fig. 7 shows clearly the transition performed with the spline interpolation in PSTAR from Eq. (7) to the Bethe-Bloch formula between $E_{R1} = 0.75$ MeV and $E_{R2} = 2.0$ MeV and the quality of the agreement with the data depends on the energy. Above ∼2 MeV, where the modern Bethe-Bloch expression is adopted by PSTAR, the agreement with the measurements is rather good. Below ∼2 MeV, PSTAR deviates from the experiment: this is the region of the spline interpolation adjusted without a theoretical guidance or a fit to experimental data. The deviations given in Table IV show the essential comparable performance of SRIM and PSTAR.

CASP is a code build on the perturbative convolution approximation (PCA) and the improved unitary convolution approximation (UCA) developed by Grande and Schiwietz [58,78]. The trajectory of the projectile colliding with a target atom is approximated by a straight line (which is equivalent to neglecting the nuclear stopping power and is not an important limitation in the present energy range) and can hence be characterized uniquely by an impact parameter vector $\boldsymbol{b}$. In an independent electron description, the convolution approximation gives the contribution $S_k(b)$ of the kth electron to the stopping cross section as

$$S_k(b) = \int d^2r_\perp \, T_k(\boldsymbol{b} - \boldsymbol{r}_\perp) \int dr_\parallel \, \rho_k(\boldsymbol{r}_\perp, r_\parallel), \qquad (9)$$

where the distance vector to the nucleus $\boldsymbol{r}$ has been decomposed in two parts: one perpendicular $\boldsymbol{r}_\perp$ and one parallel $r_\parallel$ to the impact parameter vector $\boldsymbol{b}$ (see Refs. [58,78] for more details). The second term $\int dr_\parallel \, \rho_k(\boldsymbol{r}_\perp, r_\parallel)$ is the integrated charge density of the kth electron along the impinging projectile trajectory. The quantity $T_k(\boldsymbol{b}_e)$ is the average energy transferred to the kth electron by the projectile when its impact parameter relative to the electron is $\boldsymbol{b}_e = \boldsymbol{b} - \boldsymbol{r}_\perp$. $T(\boldsymbol{b}_e)$

represents most of the physical content of the model and cannot be calculated in closed form without further approximations.

Schiwietz and Grande proposed an analytic formula, called the perturbative convolution approximation (PCA) [58], that can correctly reproduce the exact low and high energy limits; moreover once inserted into Eq. (9) and integrated over all impact parameters, it gives, as a high-velocity limit, the Bethe formula. As in the Bethe formula, the knowledge of the energies and the oscillator strengths of the transitions for each subshell of the target atom are necessary in the expression of $T_k(\boldsymbol{b}_e)$. If this information is not supplied to the program, $T_k(\boldsymbol{b}_e)$ is obtained from an approximation requiring only the binding energy of each subshell and the mean ionization potential I_{Bethe} of the Bethe-Bloch formula.

In a later work [78], Schiwietz and Grande further improved the expression of $T_i(\boldsymbol{b}_e)$ in such a way that once inserted into Eq. (9) and integrated over all impact parameters, it gives the Bethe formula with the discussed Bloch correction as a high-velocity limit. This is called the unitary convolution approximation (UCA) and is the recommended default choice to compare with experimental data. Finally, the expression of $T_k(\boldsymbol{b}_e)$ in the UCA was recently [79] improved to incorporate corrections related to the Barkas and Shell ones already discussed.

The last parameter entering the calculation of the stopping power in CASP is the charge state of the projectile: a parametrization of the measurements is generally used [80], while in some cases the experimental values are taken directly [79]. Moreover, CASP allows the user to specify the charge state, an option that can be quite useful in situations where the equilibrium is not present. For clarity, we remind the reader that protons with the energies considered here are however always fully stripped and these features of CASP are not probed by the present data.

The results from CASP version 5.2 downloaded in April 2015 are compared with the present data in Fig. 7. As recommended by the developers of CASP, the UCA approximation and the "charge state scan" options have been selected during the evaluations. The mean ionization potential of whole atoms I_{Bethe} are taken from the ICRU 37 report and all other options are default. In particular, no specific table of the oscillator strengths for each sub-shell of Al or Mo has been supplied to the program. For Al, Fig. 7(a), there is a clear tendency to underestimate the energy loss by $\sim -2\%$ at $\sim$3.5 MeV worsening to $\sim -5\%$ at $\sim$1 MeV. Al is a reference material whose I_{Bethe} is very well known [67] and has a low atomic number, implying weaker shell corrections; it should be the easiest case. However, for Mo, Fig. 7(b), the situation is better and the calculation of the stopping power agrees with the current data at $\sim$1.5% for approximately all energies covered in this plot (0.5 MeV up to 5.0 MeV). Table IV summarizes this comparison. No detailed claims on the accuracy of CASP can be found in the publications describing the method [58,78,79]. Typical deviations reported by CASP [79] are of the order of 10%, increasing to 20% at low energies of the $\sim$50 keV. If an accuracy better than 10% is sought, the default approximation relaying on the binding energy of the subshells and on I_{Bethe} has to be dropped [58]. Both statements are consistent with the present findings, and an increasing of the discrepancy between the data and CASP towards lower energies was found. In general, it is expected that semiempirical models, i.e., belonging to class (i), perform better than simplified models, belonging to class (ii), because the former incorporate in more or less refined ways the data themselves (see also Table IV).

B. Comparison with GEANT 3 and GEANT 4

As a last comparison, the original GEANT 3 [81] and its successor GEANT 4 [82] will be considered in the present section. The GEANT toolkit (abbreviation of "GEometry ANd Tracking") is a general purpose Monte Carlo code widely employed to simulate the passage of particles (photons, electrons, protons, charged hadrons, high-Z ions, and neutrons) through matter, covering a wide energy range. GEANT 4 was developed to model the response of the big and complex detectors installed at the CERN LHC accelerator, and for this reason its main emphasis is on high-energy particles. More recently, however, it is being used in medical physics and has been used for space applications as well. Here, we want to test these models and investigate its accuracy in the energy range of interest for IBA. Specific improvements to model the stopping power of heavy ions, mostly based on the ICRU 73 [83] report, introduced by Lechner *et al.* [84,85], as well as special extensions of GEANT 4 for the evaluation of dose effects at the cellular level (GEANT 4–DNA [86]) and for simulating the response of microelectronic devices to radiation (GEANT 4–MICROELEC) were recently added, but will not be covered here. Our focus is the stopping powers of protons in the few-MeV energy range calculated with the common framework available in the standard and low-energy extensions of GEANT 4 version 10.1 released in December 2014. In GEANT 4, the stopping power of a singly charged generic hadron with kinetic energy E_{hadron} is given by the stopping power of a base particle through a scaling relation to the base particle kinetic energy E_{base} as

$$E_{\text{base}} = E_{\text{hadron}} \frac{m_{\text{base}}}{m_{\text{hadron}}}, \tag{10}$$

where m_{hadron} and m_{base} are the masses of the hadron and base particle, respectively. For all singly charged hadrons with spin, with positive or negative charge, the base particle is a proton or an antiproton, respectively [87].

GEANT 4 uses for the energy loss of protons a more or less semiempirical parametrization, which is divided, for reasons of accuracy, into a lower and an upper region, separated by a limiting kinetic energy E_{lim} [87]. The two functions, $S_{\text{L}}(E)$ and $S_{\text{H}}(E)$, are combined into a single continuous curve $S(E)$ by

$$\begin{aligned} &S_{\text{L}}(E), \quad E \leqslant E_{\text{lim}}, \\ &S_{\text{H}}(E) + [S_{\text{L}}(E_{\text{lim}}) - S_{\text{H}}(E_{\text{lim}})] \frac{E_{\text{lim}}}{E}, \quad E > E_{\text{lim}}. \end{aligned} \tag{11}$$

The default value of E_{lim} is 2 MeV, almost in the middle of the energy region covered by the present data. The high-energy part S_{H} is given by the Bethe-Bloch expression with the I_{Bethe} taken from the ICRU 37. S_{H} includes several improvements: (a) the shell correction (the same model as in the ICRU 37), (b) the Bloch and Barkas corrections (following the original work by Bloch and the theory by Ashley, Ritchie, and Brandt, respectively, again as in the ICRU 37), (c) the density correction (using the treatment by Sternheimer [71,72]

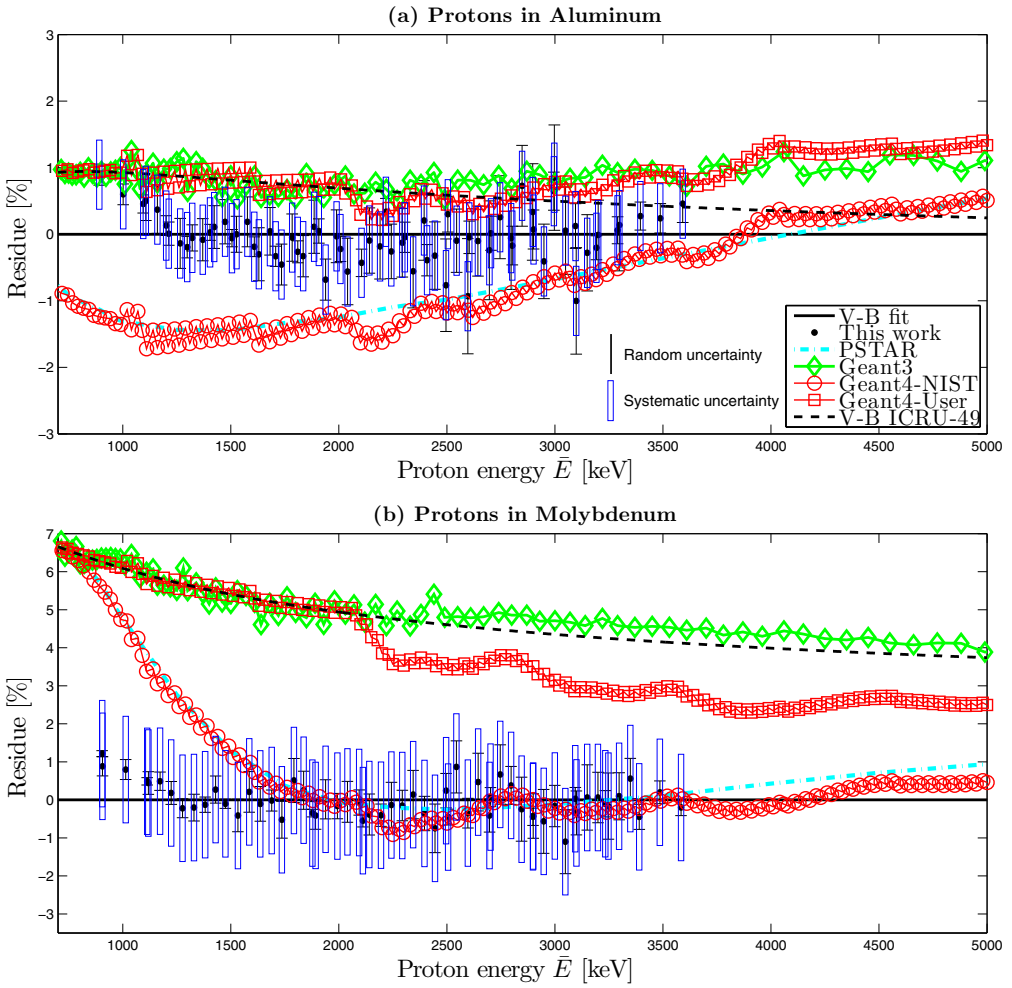

FIG. 8. Comparison between the present data (solid circles) and evaluations performed with the GEANT series for Al and Mo [panels (a) and (b), respectively]. The same representation of the residuals from the VB parametrization Eq. (7), as in Figs. 6 and 7, has been adopted to show small deviations. Because of how the energy loss is parametrized in GEANT 4, it is interesting to include in the same figures the values calculated with PSTAR (dash-dotted line) and with Eq. (7) adopting the parameters from ICRU 49 (dashed line; see text for details).

once more as in the ICRU 37), (d) the Mott correction [88], and (e) a finite-size correction [88]. Effect (e) accounts for the charge distribution inside each hadron and violates the simple scaling given in Eq. (10), but it is important only above several GeV, and is of no concern here. Effects (c) and (d) are only relevant for high projectile velocities. More details can be found in the GEANT 4 physics reference manual [87]. For the present discussion (a) and (b) are the most important; hence the implementation of GEANT 4 agrees with the ICRU 37 and with the ICRU 49. Below $E_{\rm lim}$, where atomic structure details become increasingly important invalidating the Bethe-Bloch theory, two choices are provided by GEANT 4 depending on how the material is defined. If it is selected from a predefined default list of 74 materials, called NIST materials, the PSTAR parametrization is adopted. If the material is manually defined by its elemental composition, the VB parametrization is automatically selected, with the coefficients taken from the ICRU 49 report. In the GEANT 4 implementation, the stopping power for hadrons is calculated inside the electromagnetic process G4HIONISATION, which in turn instantiates the models G4BETHEBLOCHMODEL and G4BRAGGMODEL to calculate $S_{\rm H}$ and $S_{\rm L}$, respectively.

The present data have been compared with the stopping power calculated by GEANT 4 in Fig. 8, using the residuals from the VB parametrization Eq. (7) with the parameters from Sec. III C following consistently the same procedure which has been employed in Figs. 6 and 7. The materials have been defined either by the default GEANT 4 list (NIST material) or explicitly introducing the material as a pure element (user defined). The values of the electronic stopping cross section were extracted by instantiating the G4EMCALCULATOR CLASS and calling the COMPUTEELECTRONICDEDX method. A very high energy cut has been set for the emission of δ rays. The GEANT 4 internal energy loss tables have been initialized with 40 points per decade (the default is 7) and the interpolation method has been set to spline (the default). From the previous introduction, it is clear that it is interesting to compare the direct evaluation of PSTAR and the VB parametrization Eq. (7) with the coefficients from the ICRU 49. As explained in Sec. IV A, the ICRU 49 does not employ Eq. (7) above

$E_{R1} = 0.3$ MeV for Al and $E_{R1} = 0.75$ MeV for Mo: there is no contradiction between the statement made in Sec. IV A that PSTAR and the ICRU 49 agree and the two different curves shown in Fig. 8, because the latter refers to Eq. (7) with the ICRU 49 coefficients extended at all energies. Below $E_{lim} = 2$ MeV, GEANT 4 with the NIST material agrees with PSTAR and GEANT 4 with the user-defined materials agrees with Eq. (7) with the ICRU 49 coefficients. The oscillations are most probably due to the interpolation of the internal GEANT 4 tables. In the case of Mo, the transition at E_{lim} in Eq. (11) is particularly visible; in fact Eq. (11) grants the continuity of the function, but not of its derivatives. Moreover, Eq. (11) does not switch immediately to the Bethe-Bloch expression above E_{lim} but implements a soft transition (contrary to PSTAR which is purely Bethe-Bloch for $E > E_{R2} = 1.0$ MeV and 2.0 MeV in Al and Mo, respectively): the difference between GEANT 4 with the NIST and the user-defined materials fades away slowly. Considering the data, it can be concluded that for Al there is a reasonable agreement with GEANT 4 within the error bars, with a preference for the user material in practically all the energy range considered here. For Mo, the NIST material is better above ~1.3 MeV. Below ~1.3 MeV neither of them is particularly good. More quantitative information is given in Table IV following the same procedure adopted in the last subsection for theoretical calculations. It can be seen that GEANT 4, if the NIST material is selected, is generally close to PSTAR on which it is based.

For completeness, the stopping cross sections from GEANT 3, the previous version of GEANT developed at CERN during the LEP era, has also been included in the figures. The last release of GEANT 3, version 3.21/14, has been used. GEANT 3 agrees well with GEANT 4 for the user-defined materials.

V. CONCLUSIONS AND OUTLOOK

The experimental stopping cross sections of Al and Mo for protons have been measured in the energy range of 0.9–3.6 MeV, using the transmission method with high accuracy: 0.63% (0.32% random and 0.54% systematic) for Al and 1.5% (0.44% random and 1.4% systematic) for Mo, respectively. These errors were estimated by carefully designed protocols to track down all uncertainties of the experimental data. The final results are reported as a text file in the Supplemental Material [31], with the uncertainties separated into random and systematic.

The Varelas-Biersack parametrization has been used to subtract the gross behavior common to all measurements and to plot the data in a rather expanded scale. In particular, the Al results obtained in this work were compared with 131 others from the database by Paul [30] and a good agreement was found confirming the validity of our procedure. For Mo, published measurements are limited (only 20 data points again from the database by Paul fall within the energy range studied in this work) and our results significantly increase the existing data.

The oldest and the newest version of the SRIM code (SRIM 1985 and SRIM 2013, respectively) are in very good agreement with the present data for Al, with an average agreement Δ_{PS} of 0.91% and −0.22% for SRIM 1985 and for SRIM 2013, respectively. For Mo, the newest version agrees better with our data (−0.33%) than SRIM 1985 (1.7%), indicating an update of the SRIM database. The PSTAR program deviates on average by 1.0% and −0.6% for Al and Mo, respectively. Because of the way the energy loss is parametrized in PSTAR, with a low and a high energy region, the agreement for Mo improves drastically above ~1.5 MeV. We also pointed out that for the CASP 5.2 software, without any additional experimental or theoretical information on oscillator strengths, the average deviation is 2.9% and −1.5% for Al and Mo, respectively.

The data from the current paper were also compared to the stopping cross sections evaluated by GEANT 3 and GEANT 4. The average agreement of GEANT 3 was considered good for Al (−0.80%), and worse for Mo (−4.8%), essentially energy independent. A similar tendency to overestimate the energy loss is apparent for GEANT 4 in the Al case, when the material is taken from the NIST database: the average discrepancy is −0.67% while for Mo the average discrepancy is worse −4.1%. If the same material is explicitly defined by the user, for the Al the average difference slightly worsens to 1.2%, while in contrast, for the Mo case, it improves to −0.53%. However, for Mo in energy region below ~1.5 MeV GEANT 4 (and GEANT 3 and PSTAR) depart strongly from the data, reaching a maximum deviation of ~6% at the lowest energy covered by the present measurements. Nowadays, a large collection of processes necessary to describe the propagation of many particle species have already been implemented in GEANT 4. It is our feeling that its evolution has reached a mature stage where a detailed benchmarking of its features openly available to its users would be important to enable them to judge the reliability of the results. Until this labor-intensive task is undertaken by the developers, we urge users, in particular those from the medical community and especially if they anticipate that stopping powers for few-MeV protons with accuracies below ~5% are necessary for their application, to perform the benchmarking themselves for the materials, energies, and models of interest. The freely available database by Paul, which has also been used in the present work, is an important resource to avoid directly scanning the huge literature on experimental results.

The analysis of the budget of uncertainty here presented indicates that the main limitation to further reduce the uncertainty below 1% is the quality of the target foils. This is possibly a general conclusion, at least in the energy region of a few MeV, where the transmission method is employed with commercial grade foils. Other methods could eventually be employed with different target fabrication techniques (such as thin-film deposition), but a quantitative comparison of the achievable accuracy will only be possible after a compilation of its budget of uncertainties.

ACKNOWLEDGMENTS

The authors acknowledge financial support from the Brazilian federal funding agencies CNPq and CAPES and the São Paulo state funding agency FAPESP under Contract No. FAPESP2013/09105-0. The authors also thank the Laboratory of Ion Beam Analysis of the University of São Paulo (LAMFI-USP) for the beam time, Marcos A. Rodrigues for operating the accelerator, and W. A. Engel for assistance with the targets.

[1] R. Ullah, F. Corsetti, D. Sanchez-Portal, and E. Artacho, Phys. Rev. B **91**, 125203 (2015).

[2] R. Miksova, V. Hnatowicz, A. Macková, P. Malinsky, and P. Slepicka, Nucl. Instrum. Methods Phys. Res., Sect. B **354**, 205 (2015).

[3] C. A. Rios Rubiano, G. A. Bocan, J. I. Juaristi, and M. S. Gravielle, Phys. Rev. A **89**, 032706 (2014).

[4] E. D. Cantero, R. C. Fadanelli, C. C. Montanari, M. Behar, J. C. Eckardt, G. H. Lantschner, J. E. Miraglia, and N. R. Arista, Phys. Rev. A **79**, 042904 (2009).

[5] A. V. Solov'yov, E. Surdutovich, E. Scifoni, I. Mishustin, and W. Greiner, Phys. Rev. E **79**, 011909 (2009).

[6] Y. J. Ma, F. Lu, J. J. Yin, and C. D. Ma, Mater. Sci. Eng. B **178**, 1464 (2013).

[7] M. Msimanga, C. B. Mtshali, and C. A. Pineda-Vargas, Nucl. Instrum. Methods Phys. Res., Sect. B **349**, 1 (2015).

[8] D. Moussa, S. Damache, and S. Ouichaoui, Nucl. Instrum. Methods Phys. Res., Sect. B **343**, 44 (2015).

[9] N. P. Barradas, E. Alves, M. Fonseca, Z. Siketic, and I. B. Radovic, Nucl. Instrum. Methods Phys. Res., Sect. B **332**, 152 (2014).

[10] M. Zier, U. Reinholz, H. Riesemeier, M. Radtke, and F. Munnik, Nucl. Instrum. Methods Phys. Res., Sect. B **273**, 18 (2012).

[11] E. Rauhala, N. P. Barradas, S. Fazinic, M. Mayer, E. Szilagyi, and M. Thompson, Nucl. Instrum. Methods Phys. Res., Sect. B **244**, 436 (2006).

[12] O. N. Rosmej, A. Blazevic, S. Korostiy, R. Bock, D. H. H. Hoffmann, S. A. Pikuz, V. P. Efremov, V. E. Fortov, A. Fertman, T. Mutin, T. A. Pikuz, and A. Y. Faenov, Phys. Rev. A **72**, 052901 (2005).

[13] Y. Wang and M. Nastasi, *Handbook of Modern Ion Beam Materials Analysis*, 2nd ed. (Materials Research Society, Warrendale, PA, 2009).

[14] C. Jeynes, M. J. Bailey, N. J. Bright, M. E. Christopher, G. W. Grime, B. N. Jones, V. V. Palitsin, and R. P. Webb, Nucl. Instrum. Methods Phys. Res., Sect. B **271**, 107 (2012).

[15] T. F. Silva, M. V. Moro, G. F. Trindade, N. Added, M. H. Tabacniks, R. J. Santos, P. L. Santana, and J. R. R. Bortoleto, Thin Solid Films **545**, 171 (2013).

[16] N. P. Barradas, K. Arstila, G. Battistig, M. Bianconi, N. Dytlewski, C. Jeynes, E. Kotai, G. Lulli, M. Mayer, E. Rauhala, E. Szilagyi, and M. Thompson, Nucl. Instrum. Methods Phys. Res., Sect. B **266**, 1338 (2008).

[17] K. A. Sjöland, F. Munnik, and U. Wätjen, Nucl. Instrum. Methods Phys. Res., Sect. B **161-163**, 275 (2000).

[18] C. Jeynes, N. P. Barradas, and E. Szilagyi, Anal. Chem. **84**, 6061 (2012).

[19] J. L. Colaux and C. Jeynes, Anal. Methods **6**, 120 (2014).

[20] H. Paganetti, H. Y. Jiang, K. Parodi, R. Parodi, R. Slopsema, and M. Engelsman, Phys. Med. Biol. **53**, 4825 (2008).

[21] A. Itoh, M. Kaneda, M. Shimizu, T. Hayakawa, T. Iriki, and H. Tsuchida, Vacuum **84**, 999 (2010).

[22] M. Shimizu, T. Hayakawa, M. Kaneda, H. Tsuchida, and A. Itoh, Vacuum **84**, 1002 (2010).

[23] T. Siiskonen, H. Kettunen, K. Perajarvi, A. Javanainen, M. Rossi, W. H. Trzaska, J. Turunen, and A. Virtanen, Phys. Med. Biol. **56**, 2367 (2011).

[24] S. Limandri, P. de Vera, R. C. Fadanelli, L. C. C. M. Nagamine, A. Mello, R. Garcia-Molina, M. Behar, and I. Abril, Phys. Rev. E **89**, 022703 (2014).

[25] H. Paul, Nucl. Instrum. Methods Phys. Res., Sect. B **268**, 3421 (2010).

[26] J. F. Ziegler, J. P. Biersack, and U. Littmark, *The Stopping and Range of Ions in Solids*, 1st ed. (Pergamon Press, New York, 1985).

[27] J. F. Ziegler, M. D. Ziegler, and J. P. Biersack, Nucl. Instrum. Methods Phys. Res., Sect. B **268**, 1818 (2010).

[28] H. Paul and D. Sanchez-Parcerisa, Nucl. Instrum. Methods Phys. Res., Sect. B **312**, 110 (2013).

[29] M. Mayer, W. Eckstein, H. Langhuth, F. Schiettekatte, and U. von Toussaint, Nucl. Instrum. Methods Phys. Res., Sect. B **269**, 3006 (2011).

[30] H. Paul, Stopping Power for Light Ions. Available from https://www-nds.iaea.org/stopping (accessed and downloaded February 2015).

[31] See Supplemental Material at http://link.aps.org/supplemental/10.1103/PhysRevA.93.022704 for access to the stopping cross section measured in this work.

[32] D. Goebl, W. Roessler, D. Roth, and P. Bauer, Phys. Rev. A **90**, 042706 (2014).

[33] P. Mertens, Nucl. Instrum. Methods Phys. Res., Sect. B **27**, 315 (1987).

[34] S. Damache, D. Moussa, and S. Ouichaoui, Nucl. Instrum. Methods Phys. Res., Sect. B **268**, 1759 (2010).

[35] S. Damache, S. Ouichaoui, A. Belhout, A. Medouni, and I. Toumert, Nucl. Instrum. Methods Phys. Res., Sect. B **225**, 449 (2004).

[36] L. G. Glazov, Nucl. Instrum. Methods Phys. Res., Sect. B **192**, 239 (2002).

[37] P. Sigmund and K. B. Winterbon, Nucl. Instrum. Methods Phys. Res., Sect. B **12**, 1 (1985).

[38] J. L. Colaux and C. Jeynes, Anal. Methods **7**, 3096 (2015).

[39] J. L. Colaux, G. Terwagne, and C. Jeynes, Nucl. Instrum. Methods Phys. Res., Sect. B **349**, 173 (2015).

[40] A. F. Gurbich and C. Jeynes, Nucl. Data Sheets **119**, 270 (2014).

[41] G. F. Knoll, *Radiation Detection and Measurement*, 4th ed. (John Wiley & Sons, New York, NY, 2010).

[42] C. Pascual-Izarra and N. P. Barradas, Nucl. Instrum. Methods Phys. Res., Sect. B **266**, 1866 (2008).

[43] J. Schindelin, I. Arganda-Carreras, E. Frise, V. Kaynig, M. Longair, T. Pietzsch, S. Preibisch, C. Rueden, S. Saalfeld, B. Schmid *et al.*, Nat. Methods **9**, 676 (2012).

[44] M. J. Berger, J. H. Hubbell, S. M. Seltzer, J. Chang, J. S. Coursey, R. Sukumar, D. S. Zucker, and K. Olsen. Available from http://www.nist.gov/pml/data/xcom/index.cfm (accessed February 2015).

[45] T. F. Silva, C. L. Rodrigues, M. Mayer, M. V. Moro, G. F. Trindade, F. R. Aguirre, N. Added, M. A. Rizzutto, and M. H. Tabacniks, Nucl. Instrum. Methods Phys. Res., Sect. B (2015).

[46] M. Mayer, SIMNRA, A Simulation Program for the Analysis of NRA, RBS, and ERDA, in *Proceedings of the 15th ICAARI*, edited by J. L. Duggan and I. L. Morgan, AIP Conf. Proc. No. 475 (AIP, New York, 1999), p. 541.

[47] M. Chiari, L. Giuntini, P. A. Mandò, and N. Taccetti, Nucl. Instrum. Methods Phys. Res., Sect. B **174**, 259 (2001).

[48] J. F. Ziegler, The Stopping and Range of Ions in Matter. Available from http://www.srim.org (accessed February 2015).

[49] H. H. Andersen, A. F. Garfinke, C. C. Hanke, and H. Sørensen, Kgl. Danske Videnskab. Selskab, Mat.-Fys. Medd **35**, 4 (1966).

[50] International Commission on Radiation Units and Measurements (ICRU), Report 49: Stopping Power and Ranges for Protons and Alpha Particles, 1993.

[51] Working Group of the Joint Committee for Guides in Metrology, Evaluation of Measurement Data: Guide to the Expression of Uncertainty in Measurement, 2008.

[52] J. D. Valentine and A. E. Rana, IEEE Trans. Nucl. Sci. **43**, 2501 (1996).

[53] C. Varelas and J. Biersack, Nucl. Instrum. Methods **79**, 213 (1970).

[54] H. H. Andersen and J. F. Ziegler, *Hydrogen: Stopping Powers and Ranges in All Elements*, Vol. 3 of the The Stopping and Ranges of Ions in Matter, 1st ed. (Pergamon Press, New York, NY, 1977).

[55] Working Group of the Joint Committee for Guides in Metrology, Evaluation of Measurement Data: Supplement 2 to the Guide to the Expression of Uncertainty in Measurement: Extension to Any Number of Output Quantities, 2011.

[56] M. J. Berger, J. S. Coursey, M. A. Zucker and J. Chang, PSTAR: Stopping-Power and Range Tables for Protons, http://physics.nist.gov/PhysRefData/Star/Text/PSTAR.html (accessed February 2015).

[57] J. F. Ziegler, J. Appl. Phys. **85**, 1249 (1999).

[58] P. L. Grande and G. Schiwietz, Phys. Rev. A **58**, 3796 (1998).

[59] P. Sigmund and A. Schinner, Eur. Phys. J. D **12**, 425 (2000).

[60] P. Sigmund and A. Schinner, Nucl. Instrum. Methods Phys. Res., Sect. B **195**, 64 (2002).

[61] P. Sigmund and A. Schinner, Nucl. Instrum. Methods Phys. Res., Sect. B **342**, 292 (2015).

[62] C. C. Montanari, J. E. Miraglia, S. Heredia-Avalos, R. Garcia-Molina, and I. Abril, Phys. Rev. A **75**, 022903 (2007).

[63] J. F. Ziegler, Nucl. Instrum. Methods Phys. Res., Sect. B **219-220**, 1027 (2004).

[64] W. Brandt and M. Kitagawa, Phys. Rev. B **25**, 5631 (1982).

[65] A. Mangiarotti, M. I. Lopes, M. L. Benabderrahmane, V. Chepel, A. Lindote, J. P. da Cunha, and P. Sona, Nucl. Instrum. Methods Phys. Res., Sect. A **580**, 114 (2007).

[66] H. Paul and A. Schinner, Nucl. Instrum. Methods Phys. Res., Sect. B **227**, 461 (2005).

[67] International Commission on Radiation Units and Measurements (ICRU), Report 37: Stopping Powers for Electrons and Positions, 1984.

[68] F. Bloch, Ann. Phys. **408**, 285 (1933).

[69] W. H. Barkas, W. Birnbaum, and F. M. Smith, Phys. Rev. **101**, 778 (1956).

[70] W. H. Barkas, J. N. Dyer, and H. H. Heckman, Phys. Rev. Lett. **11**, 26 (1963).

[71] R. M. Sternheimer, Phys. Rev. **88**, 851 (1952).

[72] R. M. Sternheimer, S. M. Seltzer, and M. J. Berger, Phys. Rev. B **26**, 6067 (1982).

[73] J. C. Ashley, V. E. Ritchie, and W. Brandt, Phys. Rev. B **5**, 2393 (1972).

[74] J. C. Ashley, V. E. Ritchie, and W. Brandt, Phys. Rev. A **8**, 2402 (1973).

[75] J. C. Ashley, V. E. Ritchie, and W. Brandt, Z_1^3 *Effects in the Stopping Power of Matter for Charged Particles: Tables of Functions* (National Auxiliary Publication Service, New York, 1974).

[76] H. Bichsel, Phys. Rev. A **41**, 3642 (1990).

[77] S. M. Seltzer and M. J. Berger, Int. J. Appl. Radiat. Isot. **33**, 1189 (1982).

[78] G. Schiwietz and P. L. Grande, Nucl. Instrum. Methods Phys. Res., Sect. B **153**, 1 (1999).

[79] G. Schiwietz and P. L. Grande, Nucl. Instrum. Methods Phys. Res., Sect. B **273**, 1 (2012).

[80] G. Schiwietz and P. L. Grande, Nucl. Instrum. Methods Phys. Res., Sect. B **175-177**, 125 (2001).

[81] GEANT 3 Manual, *A Detector Description and Simulation Tool* (CERN Program Library Long Writeup, Geneva, Switzerland, 1994).

[82] S. Agostinelli, J. Allison, K. Amako, J. Apostolakis, H. Araujo, P. Arce, M. Asai, D. Axen, S. Banerjee, G. Barrand *et al.*, Nucl. Instrum. Methods Phys. Res., Sect. A **506**, 250 (2003).

[83] International Commission on Radiation Units and Measurements (ICRU), Report 73: Stopping of Ions Heavier Than Helium, 2005.

[84] A. Lechner and V. Ivanchenko, 2008 IEEE Nuclear Symposium Conference Record, Record No. 02-91.

[85] A. Lechner, V. N. I. Ivanchenko, and J. Knobloch, Nucl. Instrum. Methods Phys. Res., Sect. B **268**, 2343 (2010).

[86] Z. Francis, S. Incerti, M. Karamitros, H. N. Tran, and C. Villagrasa, Nucl. Instrum. Methods Phys. Res., Sect. B **269**, 2307 (2011).

[87] GEANT 4 Collaboration, Physics Reference Manual (version released for GEANT 4.10.1), December 2014.

[88] S. P. Ahlen, Rev. Mod. Phys. **52**, 121 (1980); **52**, 653 (1980).